

Electronic Supplementary Information (ESI)

Boosting the Thermoelectric Performance of PbSe through Dynamic Doping and Hierarchical Phonon Scattering

Li You, Yefeng Liu, Xin Li, Pengfei Nan, Binghui Ge, Pengfei Luo, Shanshan Pan, Yanzhong Pei, Wenqing Zhang, G. Jeffrey Snyder, Jiong Yang, Jiye Zhang,* and Jun Luo**

1. Phase identification and microstructure analysis

1.1 XRD patterns

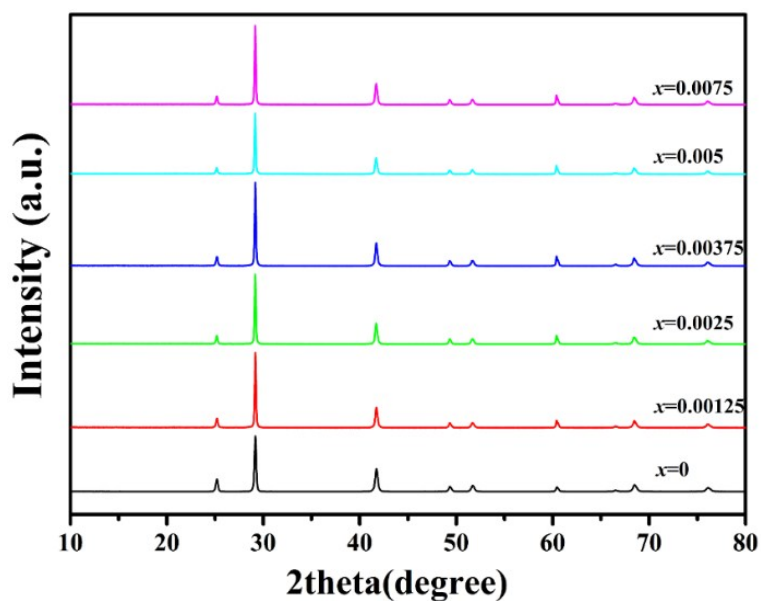


Fig. S1. Room temperature XRD patterns of PbCu_xSe samples.

XRD patterns shown in **Fig. S1** reveal that all the samples crystallize in the cubic rock-salt structure and no impurity peaks are observed. The XRD patterns do not show any obvious peak shift, indicating that the lattice parameters of our samples show no detectably changes within the uncertainty of the XRD measurement. This could be ascribed to the very small solubility of Cu in PbSe at room temperature.

1.2 Microstructure analysis

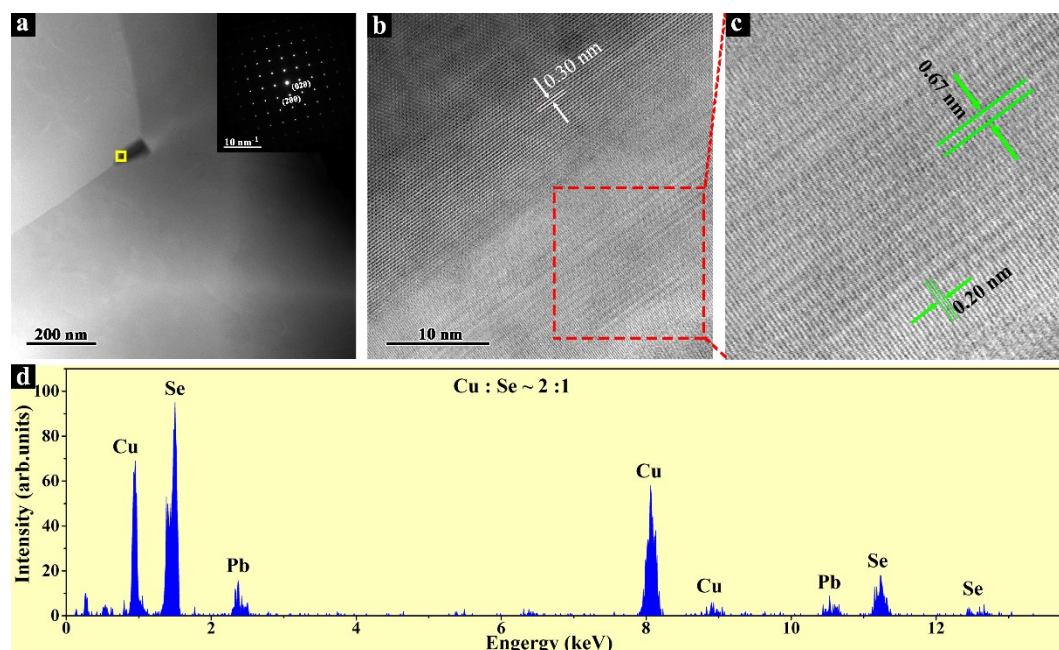


Fig. S2. Microstructure of the PbCu_xSe sample with $x=0.0075$. (a) Low-magnification HAADF-STEM image showing the nanoscale precipitate at the triangular grain boundary. The electron diffraction pattern in the inset indicates that the matrix of the sample crystallizes in the fcc structure, which can be indexed to PbSe. (b) and (c) HRTEM images of the nanoscale precipitate corresponding to the yellow region of (a). (d) EDS spectrum of the nano-precipitate in (a).

The microstructure of the phase-separated PbSe-Cu system has been examined by TEM. For clarity and simplicity, the sample with a higher Cu content (0.75 at%) has been used to illustrate the microstructure of the system at room temperature. As shown in **Fig. S2(a)**, it is obvious that the sample is composed of homogeneous host matrix and nano-sized precipitate segregating at the triangular grain boundary. The selected area electron diffraction (SAED) pattern of the matrix is shown in the inset of Fig. S2(a), which can be indexed to the [001] zone axis of PbSe. The structural feature near the precipitate is further examined by high resolution transmission electron microscopy (HRTEM). Fig. S2(b) shows the HRTEM image corresponding to the yellow rectangle area in Fig. S2(a). The spacing of 0.30 nm in Fig. S2(b) is in agreement with the (200) interplanar distance of the PbSe matrix. Fig. S2(c) shows the magnified image of the red rectangle area in Fig. S2(b), which relates to the microstructure of the Cu-rich precipitate. According to the EDS spectrum shown in Fig. S2(d), the atomic ratio of Cu to Se of the nanoscale precipitate is close to 2 : 1. The spacing of 0.67 nm corresponds to the doubled interplanar distance of the (111) plane of the high-temperature cubic Cu_2Se phase, and the lattice fringes with a spacing of 0.20 nm correspond to the (220)

plane of the cubic Cu_2Se . It is to note that the lattice fringes shown in Fig. 2(c) can also be indexed to the monoclinic Cu_2Se because of the closely structural relationship between the low-temperature monoclinic Cu_2Se and high-temperature cubic Cu_2Se . However, the precipitate in our sample should be solely designated as the low-temperature monoclinic Cu_2Se phase because of its typical layer structure. The presence of the lamellar fringes with a spacing of 0.67 nm is a solid proof to recognize the precipitate as the monoclinic Cu_2Se according to the previous report.^[1] Thus, it can be concluded that most of the Cu in our samples with higher Cu contents exists in the precipitate as a monoclinic Cu_2Se phase which resides at the grain boundary.

1.3 In-situ heating STEM characterization

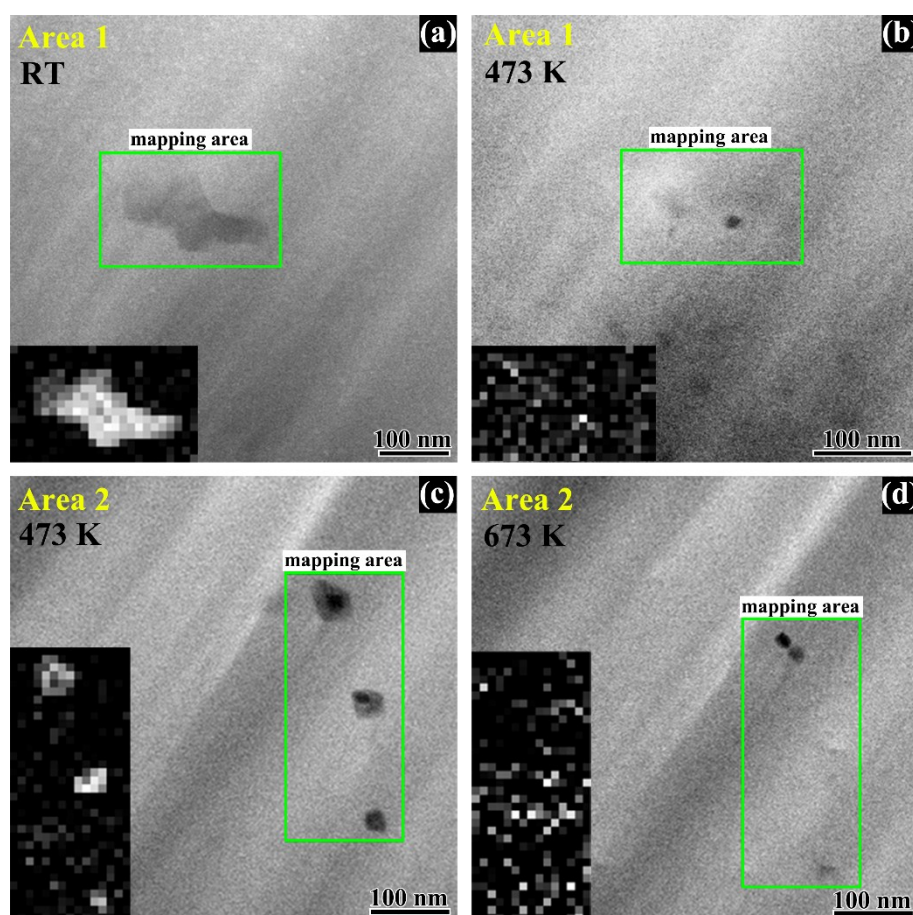


Fig. S3. (a)-(d) *In-situ* STEM image and Cu EELS mapping of Cu-rich impurities. (a) Room temperature, area 1, (b) 473 K, area 1, (c) 473 K, area 2, and (d) 673 K, area 2.

It is to note that, according to our *in-situ* STEM experiments, it is very difficult to find the second phase in our PbSe sample doped with tiny amount of Cu (less than 1

at% Cu). Therefore, we have prepared the PbCu_xSe sample with $x = 0.1$ to investigate the diffusion process of Cu at high temperatures. As shown in **Fig. S3**, the temperature dependent evolution of the Cu-rich precipitate was explored by in-situ heating STEM observation. At room temperature, we find in area 1 that a Cu-rich precipitate embeds in the PbSe matrix, as shown in Fig. S3(a). When heating to 473 K, this precipitate is almost invisible indicating the dissolving and diffusion of the Cu-rich precipitate in the PbSe matrix. This is also clearly evidenced by the corresponding Cu electron energy loss spectroscopy (EELS) mapping shown in the inset of Fig. S3(a) and (b). Since the precipitate in area 1 almost disappears, we turn to other Cu-rich precipitates in area 2 to further confirm the diffusion of Cu. As shown in Fig. S3(c), the Cu-rich precipitate at 473 K shows an obvious spreading-out feature, indicating the dissolving and diffusion of the precipitate is ongoing. The size of the precipitate becomes much smaller when the sample is heated to 673 K (Fig. S3(d)). The Cu EELS mapping shown in the inset of Fig. S3(c) and (d) shows clearly that the distribution of the Cu element becomes more uniform with the rising of temperature. Thus, the in-situ heating STEM characterization confirms the dissolving of the Cu-rich precipitate and the diffusion of Cu at high temperatures.

2. Distinction between dynamic doping effect and bipolar effect

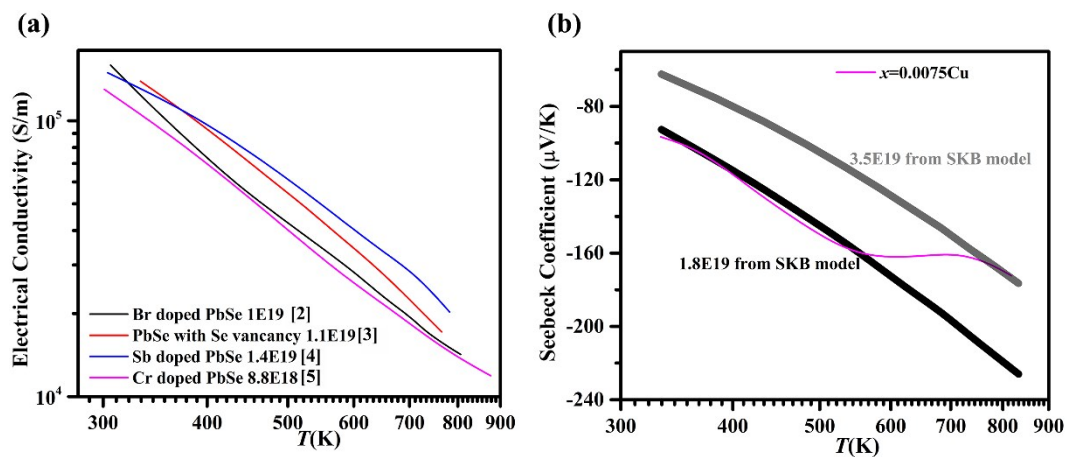


Fig. S4. (a) Temperature dependent electrical conductivities of Br,^[2] vacancy of Se,^[3] Sb,^[4] and Cr,^[5] doped PbSe samples with an initial carrier concentration close to 1×10^{19} cm⁻³ (b) Temperature dependent Seebeck coefficient of the PbCu_xSe sample with $x=0.0075$, black and gray solid line represent calculated Seebeck coefficients by the SKB model with initial carrier concentrations of 1.8×10^{19} cm⁻³ and 3.5×10^{19} cm⁻³, respectively.

It is true that both intrinsic thermal excitation (bipolar effect) and dynamic doping are all featured by the increased carrier concentration with temperature. However, for n-type PbSe, the thermal excitation of minority carrier usually comes up at a moderate temperature in a low doping level. The electron concentrations of our Cu doped PbSe samples are all above $1 \times 10^{19} \text{ cm}^{-3}$. Theoretically, as shown in **Fig. S4(a)**, intrinsic thermal excitation would not happen at this high doping level in our measured temperature range. Furthermore, according to our theoretical calculations, interstitial Cu has trivial effect on the band structure of PbSe matrix, i.e. the band gap of PbSe is not changed by doping a small amount of Cu. Thus, the increased carrier concentration at higher temperatures in our Cu doped PbSe samples should not come from intrinsic thermal excitation.

In addition, for our Cu doped PbSe samples, especially for the samples with higher Cu contents, the temperature dependent electrical conductivities and Seebeck coefficients have some unique features, distinguishing from the intrinsic thermal excitation (bipolar effect). Intrinsic thermal excitation results in increased electrical conductivity but dramatically decreased Seebeck coefficient (absolute value). However, for our Cu doped PbSe samples, their electrical conductivities first decrease with the temperature, then become flattened, and finally decrease at high temperatures. Correspondingly, the absolute values of their Seebeck coefficients first increase with the temperature, then become flattened, and finally increase at high temperatures. Besides, the Seebeck coefficient agrees well with the theoretical line calculated by single Kane band (SKB) model^[2,6] with initial carrier concentration of $1.8 \times 10^{19} \text{ cm}^{-3}$ in the low temperature range and $3.5 \times 10^{19} \text{ cm}^{-3}$ at high temperature range (see **Fig. S4(b)**). Therefore, the temperature dependent electrical conductivities and Seebeck coefficients of our PbSe samples with Cu dynamic doping are quit distinct from those caused by the intrinsic thermal excitation (bipolar effect).

3. Electronic density of states of Cu intercalated PbSe

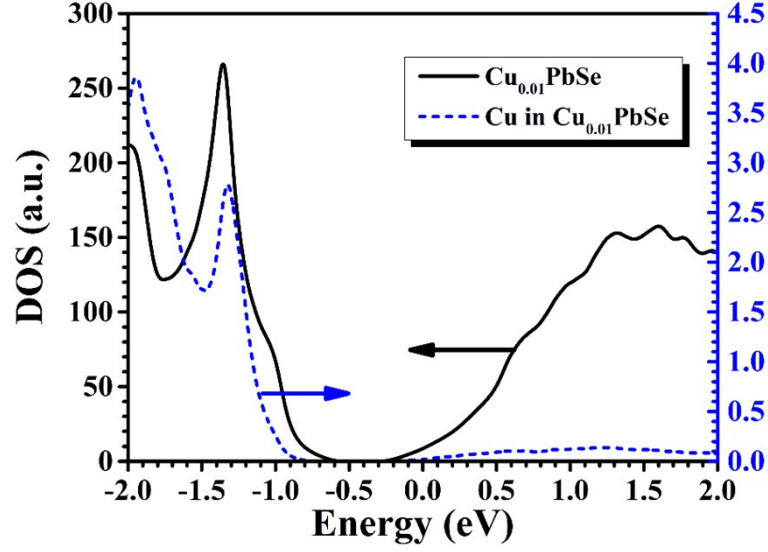


Fig. S5. Electronic density of states of 0.01 Cu intercalated PbSe. The black solid and blue dotted lines donate total DOS and partial contributions of Cu, respectively.

4. Pisarenko line and Lorenz number

The Pisarenko line and Lorenz number in semiconductors are functions of Fermi level, which can be approximately calculated by a single parabolic model with the electron-phonon interaction assumption. The employed equations for Seebeck coefficient and Lorenz number can be expressed as: [7]

$$S = \pm \frac{k_B}{e} \left(\frac{(r + 5/2)F_{r+3/2}(\eta)}{(r + 3/2)F_{r+1/2}(\eta)} - \eta \right) \quad (\text{S1})$$

$$L = \left(\frac{k_B}{e} \right)^2 \left(\frac{(r + 7/2)F_{r+5/2}(\eta)}{(r + 3/2)F_{r+3/2}(\eta)} - \left(\frac{(r + 5/2)F_{r+3/2}(\eta)}{(r + 3/2)F_{r+1/2}(\eta)} \right)^2 \right) \quad (\text{S2})$$

$$n = \frac{1}{2\pi^2} \left(\frac{2m^*k_B T}{h^2} \right)^{3/2} F_{1/2}(\eta) \quad (\text{S3})$$

$$F_i(\xi) = \int_0^\infty \frac{x^i}{1+e^{x-\xi}} dx \quad (\text{S4})$$

where S is the Seebeck coefficient, k_B the Boltzmann constant, h the reduced Planck constant, e the free electron charge, r the scattering factor, F_i the i -th Fermi integrals, η the reduced Fermi level (Fermi level over $k_B T$), n the carrier concentration, and m^* the electron effective mass. The scattering factor r is taken as $-1/2$ assuming that the acoustic phonon scattering mechanism dominates the charge transport process. The

Pisarenko relation is calculated by Equations S1, S3 and S4, and the Lorenz number can be obtained by Equation S2.

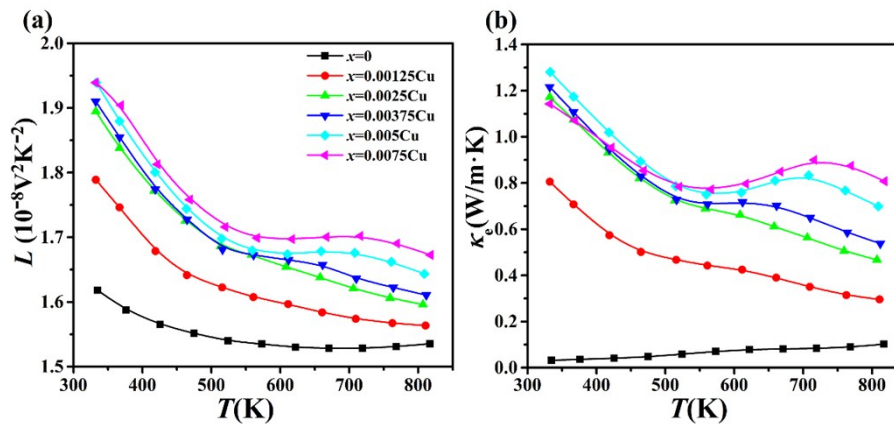


Fig. S6. Temperature dependent (a) Lorenz numbers and (b) electronic thermal conductivities of PbCu_xSe samples.

5. Dislocations and platelet like nanoclusters in Cu intercalated samples.

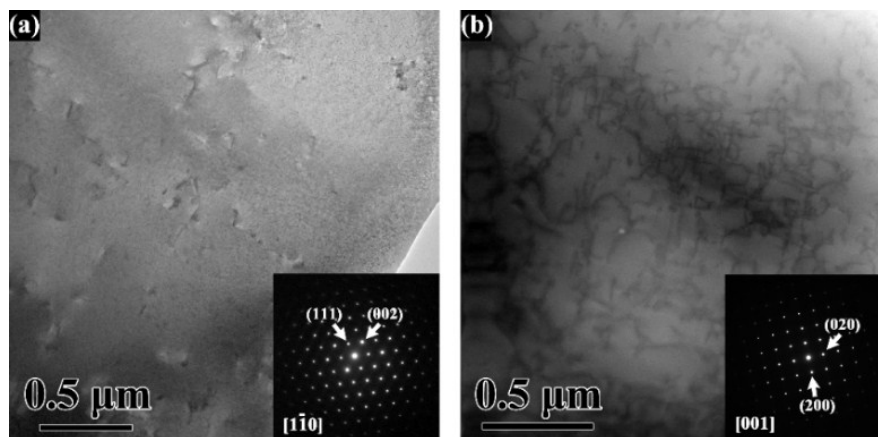


Fig. S7. Low-magnification TEM images and SAED patterns. (a) Pure PbSe sample; (b) the PbCu_xSe sample with $x = 0.75\%$.

The dislocations in the pristine PbSe and PbCu_{0.0075}Se samples were compared by low-magnification TEM. As shown in **Fig. S7**, some dislocations can be observed in the pure PbSe sample, but the dislocation density is much lower than that of the PbCu_xSe sample with $x = 0.0075$. Thus, we can conclude the dense dislocations of the 0.75 at% Cu doped PbSe sample are mainly introduced by the Cu intercalation.

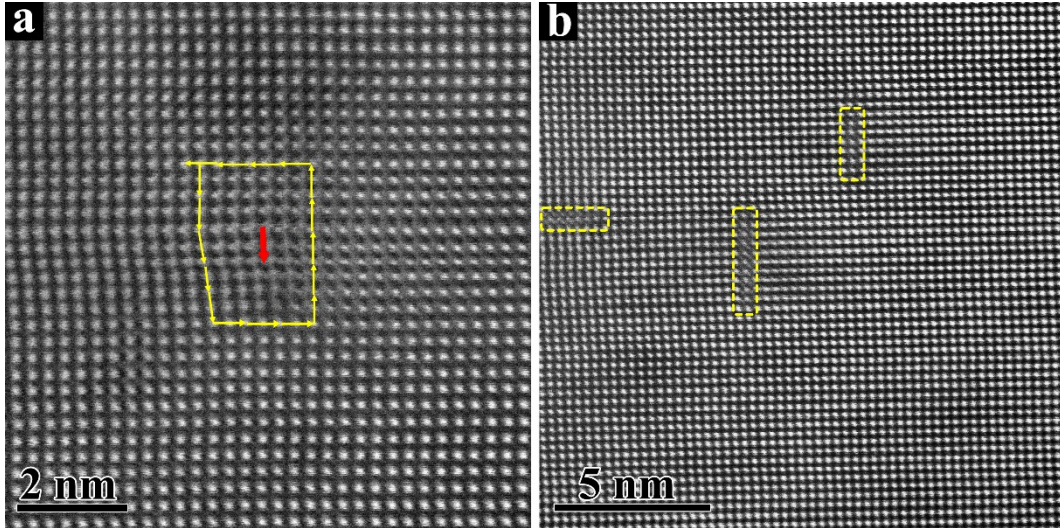


Fig. S8. HAADF STEM images of (a) a typical edge dislocation and (b) nano-clusters from ordered aggregation of interstitial atoms in the $\text{PbSeCu}_{0.075}$ sample projected along the $[001]$ direction. The yellow arrows in (a) give a complete Burgers loop of the dislocation and the red arrow denotes the extra half planes of atoms.

6. Comparison of the electrical and thermal transport properties for the PbSe systems with dynamic Cu doping and the conventional doping

6.1 Comparison of the carrier concentrations for PbSe with Cu dynamic doping and the theoretical optimized values

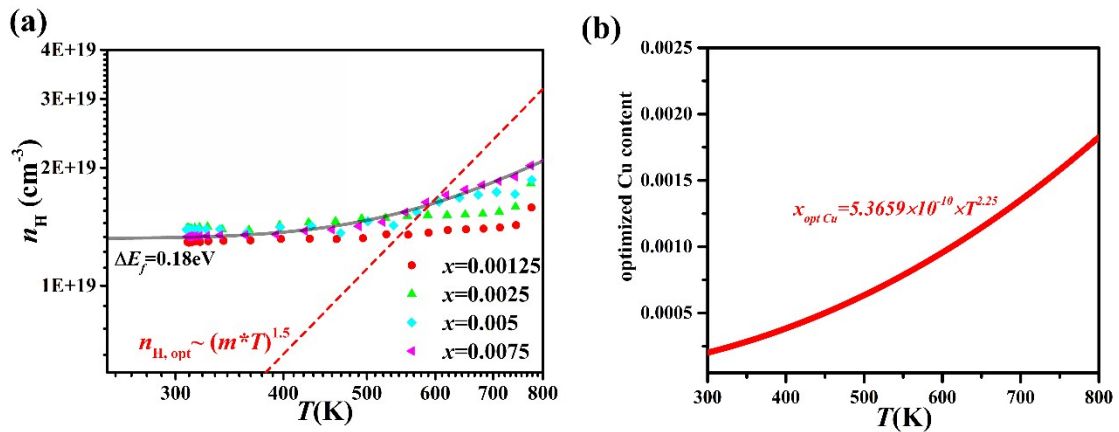


Fig. S9. (a) Temperature dependent carrier concentrations of the PbCu_xSe samples. The dash red line is the optimum carrier concentration calculated by the SKB model. (b) Optimum Cu content as a function of temperature calculated by assuming a rigid band model.

According to Ioffe's report in 1957,^[8] the optimum carrier concentration in a given thermoelectric material is not a constant but increases with the temperature. The relationship between the optimum carrier concentration and temperature can be expressed as $n_{\text{opt}} \sim (m^*T)^{1.5}$, where n_{opt} , m^* , T are the optimum carrier concentration, carrier effective mass and temperature, respectively. For the conduction band of n-type lead chalcogenide, the carrier effective mass increases as the rising of temperature with the relationship $m^* \sim T^{0.5}$ due to the band flattening at high temperatures.^[6] By adopting the SKB model^[2,6], the optimum carrier concentration at arbitrary temperature can be calculated. Finally, we can quantitatively obtain the dependence of the optimized carrier concentration on the temperature, $n_{\text{opt}} = 3.5 \times (T/300)^{2.25} \times 10^{18}$ (cm⁻³), as illustrated in **Fig. S9(a)**. Assuming that each interstitial Cu ion gives one electron to the conduction band of PbSe, the Cu content dependent carrier concentration can be theoretically calculated. Thus, the optimum Cu content at arbitrary temperature can be obtained, as shown in **Fig. S9(b)**. Based on the calculation result, we must admit that the carrier concentration of our Cu doped PbSe sample is not fully optimized in the entire temperature range. However, comparing with the conventional dopants, the strategy in the present work can indeed achieve relatively high power factor in a wide temperature range due to increased carrier concentration with the temperature. Detail analysis of the Cu induced dynamic doping and Hierarchical Phonon scattering on the electrical and thermal transport properties is shown below (section 6.2).

6.2 Optimized electrical and thermal transport properties due to Cu incorporation

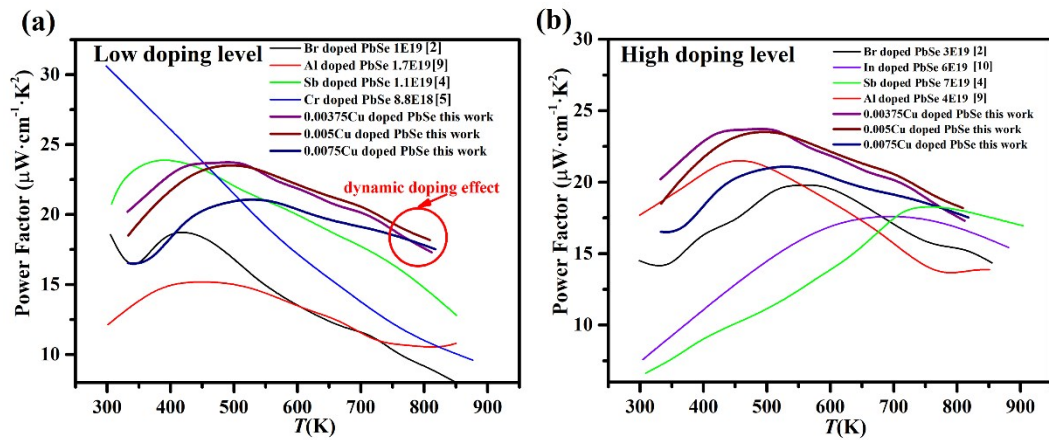


Fig. S10. Temperature dependent power factor of Br,^[2] Sb,^[4] Cr,^[5] Al,^[9] In,^[10] and Cu doped PbSe sample with different initial carrier concentrations. (a) $\sim 1 \times 10^{19}$ cm⁻³, (b) higher carrier concentration.

The outstanding thermoelectric performance in a wide temperature range in our work is achieved by the simultaneously enhanced electrical transport properties and reduced lattice thermal conductivity due to the doping of Cu. On one hand, the dynamic doping plays a significant role in the enhancement of electrical transport properties. To get a better understanding of the role of dynamic doping on the electrical transport properties enhancement, we have compared the power factor of our Cu doped PbSe samples with other n-type PbSe doped with Al, Cr, In, Br or Sb. According to the initial carrier concentration, these samples are divided into low doping level and high doping level, as shown in **Fig. S10 (a)** and **(b)**, respectively. Usually, low doping level will lead to a higher power factor in the low temperature range but a lower power factor at high temperature range. For the conventional dopants such as Al, Cr, Br, Sb, and In, the carrier densities of these doped samples do not change with the temperature (the strong degenerate case), resulting in dramatically decreased power factors at high temperatures. However, benefiting from the dynamic doping effect of intercalated Cu ions, the power factors of our samples can be maintained by the increased carrier densities at high temperatures, as shown in **Fig. S10 (a)**. In contrast, a high carrier concentration will lead to a low power factor at room temperature, as shown in **Fig. S10 (b)**. For our Cu doped PbSe samples, the carrier concentration spontaneously increases with the rising of temperature, leading to a relatively high power factor in the entire test temperature range.

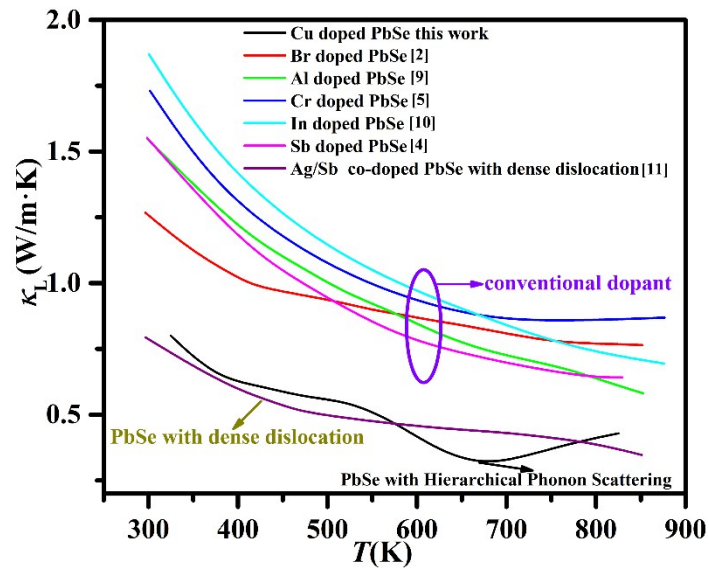


Fig. S11. Temperature dependent lattice thermal conductivities of Br,^[2] Al,^[9] Sb,^[4] Cr,^[5] In,^[10] Ag/Sb,^[11] and Cu doped PbSe sample.

On the other hand, the doping of Cu leads to complex microstructure and hierarchical phonon scattering. Therefore, ultra-low lattice thermal conductivities are achieved in our Cu doped PbSe samples, which is also responsible for the high thermoelectric performance in a wide temperature range. Compared to conventional dopants (the impurity atoms are fixed at a certain crystal site), the dense dislocations, nanoscale clusters, interstitial defects, and diffusion of Cu ions give rise to multiple phonon scattering centers in different scales, leading to reduced lattice thermal conductivities of our samples in a wide temperature range, as shown **Fig. S11**. Due to the synergistic effect of dynamic doping and hierarchical phonon scattering on the thermoelectric transport properties, outstanding zT and average zT have been simultaneously achieved because of the multiple effects of Cu in the PbSe matrix.

7. Thermoelectric properties of PbCu_xS

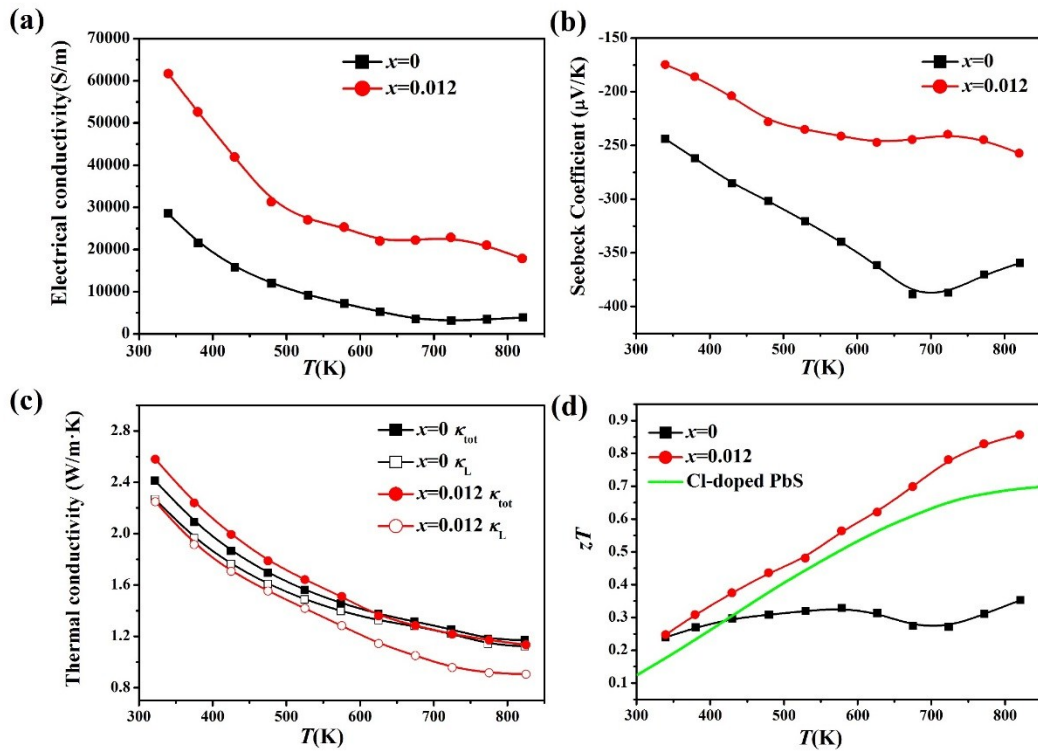


Fig. S12. Temperature dependent (a) electrical conductivity, (b) Seebeck coefficient, (c) total (κ_{tot}) and lattice thermal conductivity (κ_{L}), and (d) zT value of the PbCu_xS sample. The zT value of Cl-doped PbS shown by the green line is included for comparison.^[12]

As shown in **Fig. S12**, the temperature dependent dynamic behaviors of Cu ions are also observed in the PbCu_xS system. For the sample with $x = 0.012$, both the temperature dependent electrical conductivity and Seebeck coefficient show typical

humps at around 700 K, associating with the dissolving of Cu-rich second phase. Similar to the PbSe-Cu system, the electrical transport properties of the $\text{PbCu}_{0.012}\text{S}$ sample are optimized in a wide temperature range because of the dynamic doping effect. The intercalating of Cu into the interstitial sites of PbS provides extra electrons, leading to increased carrier concentration. Therefore, comparing with the sample free of Cu, the $\text{PbCu}_{0.012}\text{S}$ sample shows increased electrical conductivity and decreased Seebeck coefficient. In addition, the doping of Cu in the PbS lattice is responsible for the reduced lattice thermal conductivity at high temperatures, as shown in Fig. S12(c). As a result, the zT value of the Cu-intercalated PbS sample is improved.

8. Repeated measurement of thermoelectric properties and stability of the samples

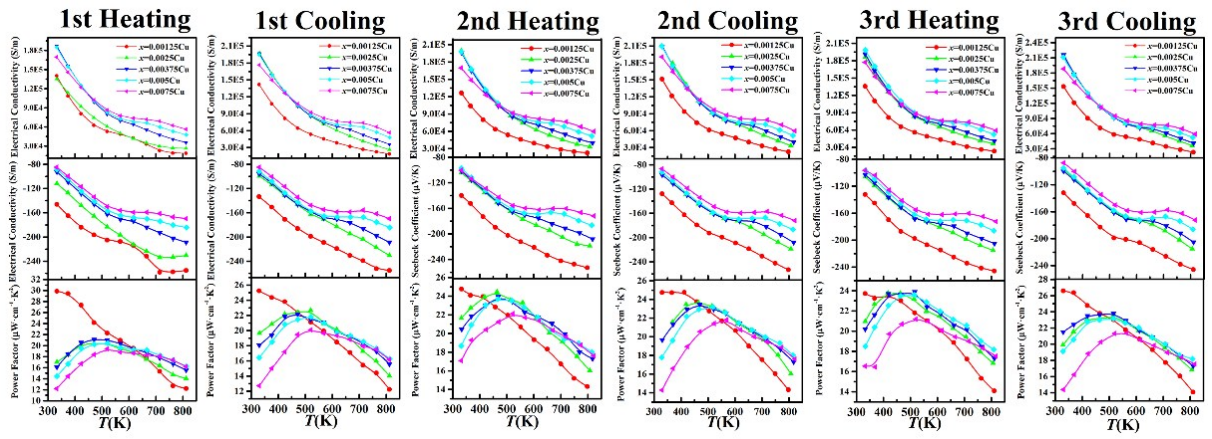


Fig. S13. Repeatedly measured temperature dependence of electrical transport properties of the PbCu_xSe samples.

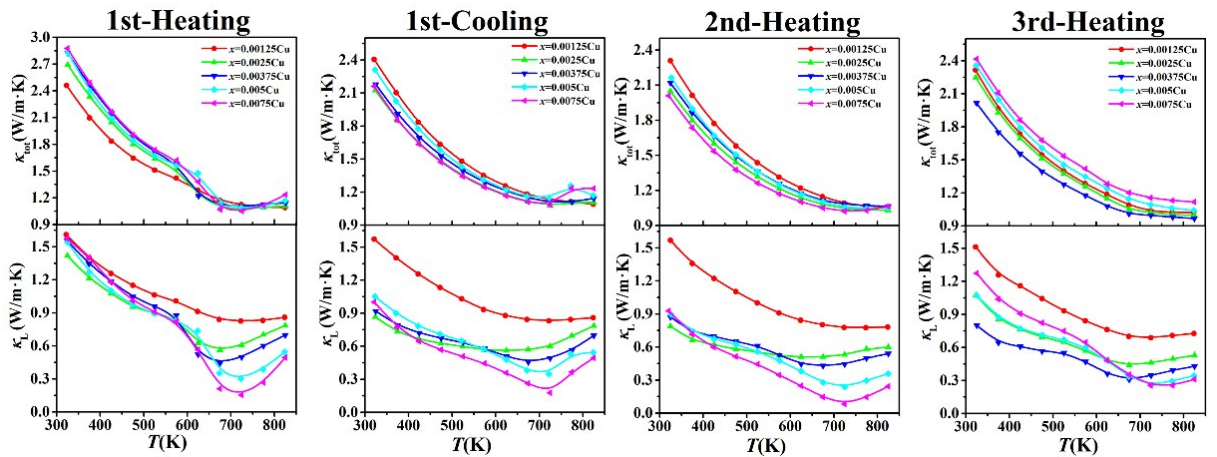


Fig. S14. Repeatedly measured temperature dependence of thermal transport properties of the PbCu_xSe samples.

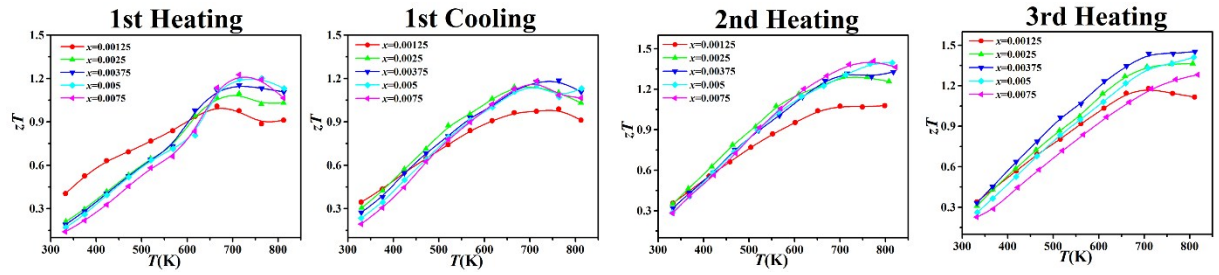


Fig. S15. Repeatedly measured zT values of the PbCu_xSe samples.

In our work, the electrical and thermal transport properties of all the samples were measured for several times in order to confirm the property reproducibility, and the experimental data presented in the manuscript were all measured during the 3rd heating process.

As shown in **Fig. S13**, our Cu doped PbSe sample shows a very good reproducibility of electrical transport properties after 4 times of non-stop cycling measurements. In addition, as shown in **Fig. S14**, the lattice thermal conductivities at high temperature (above 700 K) measured in each cycles are all decreases monotonously with the Cu concentration, which agrees well with our expectation. This can be well explained because the lattice thermal conductivities of our Cu-containing samples at high temperatures are mainly affected by the phonon alterations due to the vibrations of intercalating Cu atoms. The reproducibility of the thermal transport properties at room temperature is not as good as that at high temperatures. This might be understood based on the fact that the thermal transport properties of the samples are closely correlated to their microstructures. According to the TEM characterization, our Cu doped PbSe samples have complex microstructures including Cu_2Se nanoprecipitates, interstitial Cu atoms, and dislocations at room temperature. It is extremely difficult to precisely control these microstructures, especially the density and distribution of dislocations and nanoprecipitates. Thus, the room-temperature lattice thermal conductivity does not vary with Cu contents as expect. However, the reasonable and reproducible lattice thermal conductivity at high temperatures ensures the high thermoelectric performance of our Cu-doped PbSe samples (**Fig. S15**).

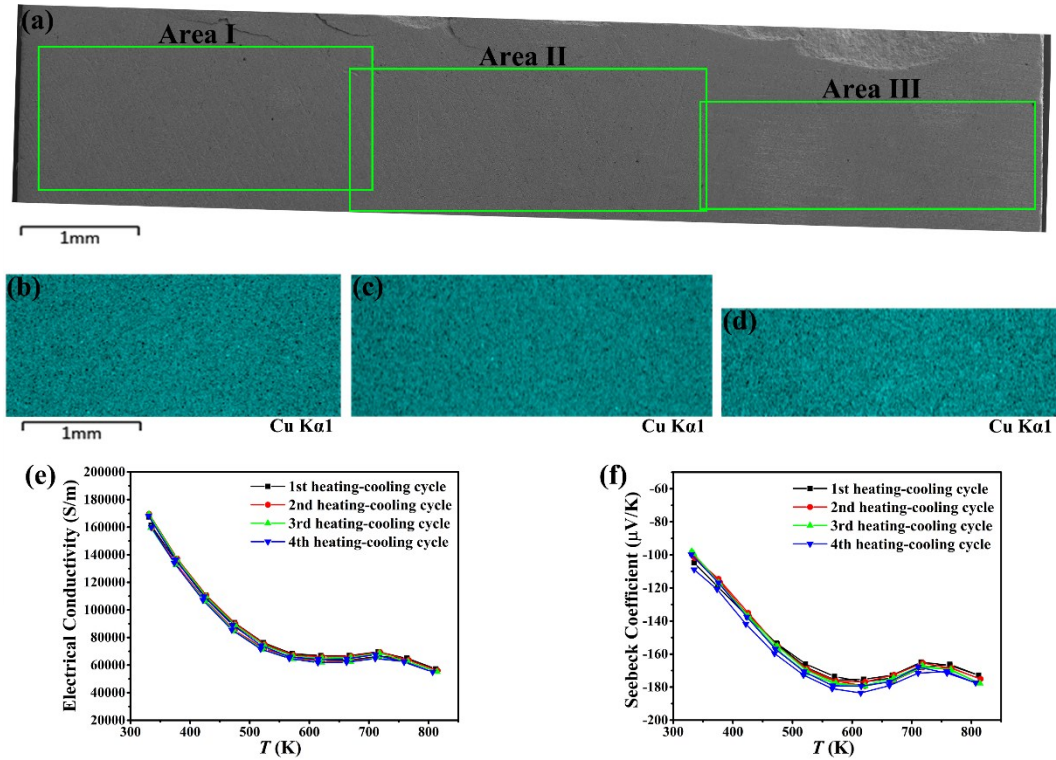


Fig. S16. (a) SEM image of the PbCu_xSe sample with $x = 0.0075$ after 4 times of non-stop cycling measurements (The image is made by splicing the SEM images for three adjacent sections of the samples). (b)~(d) is the elemental mapping of Cu for the three boxed areas labeled by green rectangles in (a) (Area I to Area III, respectively); (e) electrical conductivities and (f) Seebeck coefficients of the PbCu_xSe sample with $x = 0.0075$ measured during the heating-cooling cycles.

It is generally true that the material involving unstable crystal structure usually shows poor mechanical properties and bad stability during the cycling measurement. For example, the superionic Cu₂Se with liquid-like behavior suffers from these issues during long time operation at high temperatures, and Cu atoms diffuse out of the lattice after several times of measurements, leading to the deterioration of thermoelectric properties. However, as shown in **Fig. S16**, our Cu doped PbSe sample shows a very good reproducibility of electrical transport properties after 4 times of non-stop cycling measurements. The shape, size, and density of the sample are not changed by the cycling measurement, indicating a very good mechanical stability. According to our SEM characterization (**Fig. S16**), the composition of the repeatedly measured sample is uniform, and no aggregated Cu-related impurities can be detected at the end contacting the hot source or cold sink. This means that the Cu atoms do not migrate along the temperature gradient applied during the measurement.

We propose that the stable interstitial site of the PbSe lattice and the low content of Cu ensure the good mechanical stability and property reproducibility of our Cu doped samples. In our case, the Cu atoms mainly locate at the interstitial sites of the PbSe lattice at high temperature. Thus, because the interstitial Cu has to overcome a much higher potential barrier, it is almost impossible for the Cu atoms to diffuse out of the PbSe lattice and deposit on the contacts under the small temperature gradient applied between the hot source and cold sink during the measurement.

References

- [1] H. L. Liu, X. Shi, F. F. Xu, L. L. Zhang, W. Q. Zhang, L. D. Chen, Q. Li, C. Uher, T. Day, G. J. Snyder, *Nat. mater.* 2012, **11**, 422.
- [2] H. Wang, Y. Pei, A. D. LaLonde, G. J. Snyder, *Proc. Natl. Acad. Sci. USA* 2012, **109**, 9705.
- [3] Y. Liu, L. You, C. Wang, J. Zhang, J. Yang, K. Guo, J. Luo, W. Zhang, *J. Electron. Mater.* 2018, **47**, 2584-2590.
- [4] Y. Lee, S. H. Lo, C. Chen, H. Sun, D. Y. Chung, T. C. Chasapis, C. Uher, V. P. Dravid, M. G. Kanatzidis, *Nat. Commun.* 2014, **5**, 3640.
- [5] Q. Zhang, E. K. Chere, K. McEnaney, M. L. Yao, F. Cao, Y. Z. Ni, S. Chen, C. Opeil, G. Chen, Z. F. Ren, *Adv. Energy Mater.* 2015, **5**, 1401977.
- [6] Y. I. Ravich, B. A. Efimova, I. A. Smirnov, *Semiconducting Lead Chalcogenides*, Plenum Press, New York 1970.
- [7] G. K. Ren, S. Y. Wang, Y. C. Zhu, K. J. Ventura, X. Tan, W. Xu, Y. H. Lin, J. H. Yang, C. W. Nan, *Energy Environ. Sci.* 2017, **10**, 1590.
- [8] Ioffe, A. F. *Semiconductor Thermoelements and Thermoelectric Cooling*; Infosearch Limited: London, 1957.
- [9] Q. Zhang, H. Wang, W. Liu, H. Wang, B. Yu, Q. Zhang, Z. Tian, G. Ni, S. Lee, K. Esfarjani, G. Chen, Z. Ren, *Energy Environ. Sci.* 2012, **5**, 5246.
- [10] Q. Zhang, F. Cao, K. Lukas, W. Liu, K. Esfarjani, C. Opeil, D. Broido, D. Parker, D. J. Singh, G. Chen, Z. Ren, *J. Am. Chem. Soc.* 2012, **134**, 17731.
- [11] Z. Chen, B. Ge, W. Li, S. Lin, J. Shen, Y. Chang, R. Hanus, G. J. Snyder and Y. Pei, *Nat. Commun.* 2017, **8**, 13828.
- [12] H. Wang, E. Schechtel, Y. Pei, G. J. Snyder, *Adv. Energy Mater.* 2013, **3**, 488.